

Rolling and slipping of droplets on superhydrophobic surfaces

A. F. W. Smith,¹ K. Mahelona,² and S. C. Hendy^{1,3}

¹*MacDiarmid Institute for Advanced Materials and Nanotechnology, Department of Physics, University of Auckland, Auckland 1142, New Zealand*

²*Wai Foundation, Taipa 0483, New Zealand*

³*Te Pūnaha Matatini, Department of Physics, University of Auckland, Auckland 1142, New Zealand*



(Received 11 January 2018; revised manuscript received 23 July 2018; published 21 September 2018)

The leaves of many plants are superhydrophobic, a property that may have evolved to clean the leaves by encouraging water droplets to bead up and roll off. Superhydrophobic surfaces can also exhibit reduced friction, and liquids flowing over such surfaces have been found to slip in apparent violations of the classical no-slip boundary condition. Here we introduce slip into a model for rolling droplets on superhydrophobic surfaces and investigate under what conditions slip might be important for the steady-state motion. In particular, we examine three limiting cases in which dissipation in the rolling droplet is dominated by viscous dissipation, surface friction, or contact-line dissipation. We find that in molecular-dynamics simulations of droplets on ideal superhydrophobic surfaces with large effective slip lengths, contact-line dissipation dominates droplet motion. However, on real leaves, droplet motion is likely to be dominated by viscous shear, and slip, for the most part, can be neglected.

DOI: [10.1103/PhysRevE.98.033113](https://doi.org/10.1103/PhysRevE.98.033113)

I. INTRODUCTION

Superhydrophobic surfaces that exhibit the Lotus effect [1] are of interest both for their role in biology [2] and for their potential technological applications [3]. Superhydrophobic surfaces, including the surfaces of many plant leaves [4], combine nano- and microscale roughness with a hydrophobic surface coating to achieve contact angles of up to 160°. The Lotus effect is thought to benefit plants by helping to keep leaves clean; droplets of moisture bead up and eventually roll down leaves, entraining dirt and contaminants as they go [5]. Indeed, experiments have found that the fact that droplets roll rather than slide down superhydrophobic surfaces [6] makes them more likely to remove contamination along the way.

More recently, however, flows over superhydrophobic surfaces have been studied because they effectively violate the classical no-slip boundary condition [7]. When in the Cassie state, droplets or larger-scale flows are lubricated by an entrapped layer of air, leading to large effective slip lengths with drag only occurring at the few points of the surface where the flow makes contact with the substrate [8]. On such superhydrophobic surfaces, effective slip lengths of tenths to tens of microns have been observed [9,10], scaling proportionally to the typical microstructural length scale [10,11]. In some experiments, on highly ideal superhydrophobic surfaces, slip lengths of hundreds of microns have been measured [12].

The canonical model for the steady-state motion of small spherical droplets on superhydrophobic surfaces was proposed by Mahadevan and Pomeau [13]. This model assumes a rolling motion without slip that reaches a steady state when viscous dissipation due to shear in the vicinity of the area of contact between the droplet and the surface balances the change in gravitational potential energy. In sufficiently small droplets, however, shear stress at the surface of contact may

also generate significant slip. In this paper, we investigate the conditions under which droplets may slip as they move on superhydrophobic surfaces, whether leaves or engineered surfaces.

Mahadevan and Pomeau's model considers nearly spherical droplets supported on a superhydrophobic surface (see Fig. 1). This approximation will only be reasonable if the droplet radius is smaller than the capillary length, $\kappa^{-1} = (\gamma/\rho g)^{1/2}$ (for water $\simeq 2$ mm), where γ is the droplet surface tension, ρ is the fluid density, and g is the acceleration due to gravity. The radius of the contact zone ℓ is determined by a balance between the loss of gravitational potential energy that results from the lowering of the droplet center of mass with the corresponding creation of extra surface area. In this case, the contact zone radius ℓ can be shown to be $\sim R^2/\kappa^{-1}$ [13].

The droplets are considered to be moving on a surface tilted at an angle α to the horizontal. The center-of-mass velocity U of the droplet is equal to its rolling velocity U_r (Fig. 2), with a no-slip condition resulting in zero slip at the surface ($U_s = 0$). The shear-free rotational flow is disturbed near the contact plane, resulting in a velocity gradient $|\nabla u| \sim U/R$ and viscous dissipation over a region of size ℓ around the contact zone [13]. The rate of dissipation due to this viscous shear near the contact zone will then be given by

$$P_v = \int_V \mu (\nabla u)^2 dV = \mu \int_V \left(\frac{U}{R} \right)^2 dV \sim \frac{\ell^3 \mu U^2}{R^2}, \quad (1)$$

where the integral has been taken over the volume ($V \sim \ell^3$) about the contact zone, and μ is the shear viscosity.

In the steady state, the rate of viscous dissipation must balance the rate of loss of gravitational potential energy,

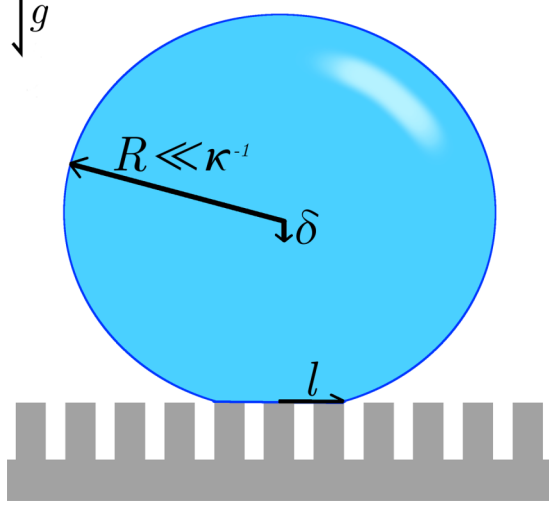


FIG. 1. A droplet in the Cassie state on a superhydrophobic surface. Although the droplet radius is below the capillary length $R \ll \kappa^{-1}$, the droplet is depressed by a distance δ by gravity (as gravitational potential energy is converted to surface energy) to form a contact zone with the surface of radius ℓ .

giving

$$\rho g R^3 U \sin(\alpha) \sim \frac{\ell^3 \mu U^2}{R^2}. \quad (2)$$

Solving for U yields the steady-state center-of-mass velocity:

$$U \sim \frac{\gamma}{\mu} \frac{\kappa^{-1}}{R} \sin(\alpha), \quad (3)$$

which shows that U scales in inverse proportion to the droplet radius R . This model should be valid for contact angles close to 180° provided the droplet radius is well below the capillary length. For droplets with a size that approaches or exceeds the capillary length or for droplets that wet the substrate, the

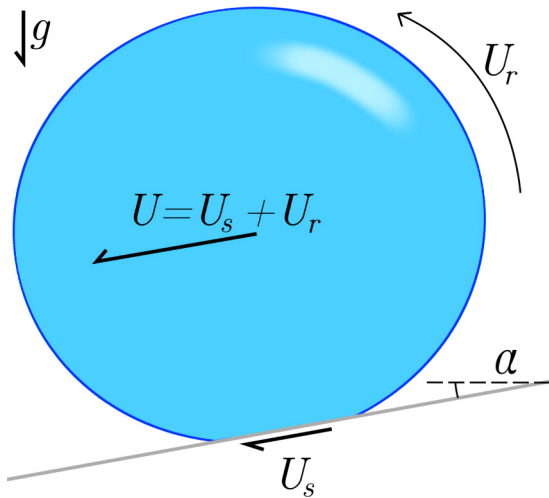


FIG. 2. A droplet rolling down a superhydrophobic surface tilted at an angle α to the horizontal with respect to the direction of the body force $m\vec{g}$. The center-of-mass velocity of the droplet, U , is assumed to be equal to the sum of rolling velocity U_r and any slip velocity U_s .

shear induced will extend beyond the contact zone, ultimately leading to different scaling predictions [14].

For small droplets on superhydrophobic surfaces, the no-slip boundary condition ($U_s = 0$) may also be a poor approximation. Indeed, some experiments have found that on highly engineered superhydrophobic surfaces, rolling can be entirely suppressed [15,16]. Other works have focused on the opposing limit, where droplet motion is constrained by pinning-depinning events or contact-line friction as the droplet progresses across the surface. These approaches vary from analysis with molecular kinetic theory [17–19] to phenomenological models (where, for example, the effect of pinning-depinning events is captured by a “sliding resistance,” tied to the droplet’s dynamic receding contact angle [20]) to consideration of the energy losses involved in the rupturing of capillary bridges found at the receding edge of the droplet [21]. Droplet motion in the presence of slip has been studied previously by simulation, but these studies have generally either not explicitly considered superhydrophobic structures [22,23], or they were restricted to two dimensions [24–26], which affects both droplet dynamics and the spectrum of available surface geometries. A recent study [27] in three dimensions simulated droplet motion using a continuum approach, but applied an effective slip boundary condition that only indirectly includes the effects of surface microstructure.

In this paper, we report on three-dimensional molecular-dynamics simulations of the motion of droplets on superhydrophobic surfaces and extensions of Mahadevan and Pomeau’s model to include slip, while considering the role of surface friction and contact-line dissipation. In particular, we have conducted molecular-dynamics simulations of droplets moving in steady state on a superhydrophobic surface in response to a gravitational force. The simulations allow us to identify a regime where the speed of the droplets is proportional to droplet size, rather than the inverse of the droplet size as given by Eq. (3). We extend this model [13] to incorporate an effective Navier slip boundary condition [28]. We also consider scenarios in which the steady-state motion of the droplet is either dominated by friction at the solid-liquid interface or by dissipation at the contact line. We show that it is most likely the latter mechanism that limits the steady-state motion of the simulated droplets.

II. MOLECULAR-DYNAMICS SIMULATIONS

Molecular-dynamics simulations of simple liquid droplets on superhydrophobic surfaces were carried out using LAMMPS [29]. The liquid and surface were modeled using the Lennard-Jones 6-12 potential:

$$V(r) = 4\epsilon \left[\left(\frac{\sigma}{r} \right)^{12} - \left(\frac{\sigma}{r} \right)^6 \right]. \quad (4)$$

In what follows, we work in Lennard-Jones units, where ϵ_{LL} is set to 1 (i.e., $\epsilon_{LL} = \epsilon$). We also used Lennard-Jones potentials to model droplet-substrate interactions with $0.05\epsilon < \epsilon_{SL} < 0.14\epsilon$. Altering ϵ_{SL} affects the observed contact angle and would be expected to alter the effective slip length of the surface. We find static contact angles between $\sim 140^\circ$ for $\epsilon_{SL} = 0.14\epsilon$ and $\sim 160^\circ$ for $\epsilon_{SL} = 0.05\epsilon$, consistent with previous results [30]. Droplet motion is driven by a small body force,

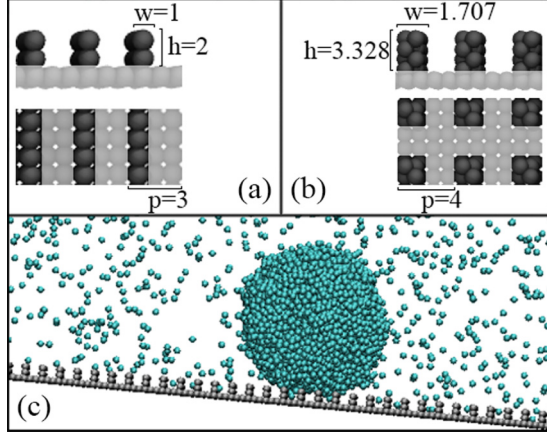


FIG. 3. The height h , width w , and period L of the surface features for the ridged (a) and pillared (b) surfaces are presented above, with all values given in terms of the lattice spacing σ . The particle diameter is shown as 1σ , matching the lattice spacing. Part (c) shows a snapshot of a simulated droplet ($R = 10\sigma$) rolling in the Cassie state on a ridged superhydrophobic surface. Although the droplet radius is below the capillary length $R \ll \kappa^{-1}$, the droplet is compressed a distance δ by gravity (gravitational potential energy is converted to surface energy) to form a contact zone with the surface of radius ℓ , spanning multiple surface features. The image is rotated so that the applied body force is directed vertically down.

between $5.7 \times 10^{-5} \sigma \tau^{-2}$ and $4.6 \times 10^{-3} \sigma \tau^{-2}$. This force is applied at an angle of $\alpha = 10^\circ$ from the vertical to mimic the effects of tilting the surface relative to the gravitational direction. This range of parameters ensures that Weber and Capillary numbers are less than unity in the simulations, so we expect the droplets to remain quasispherical. Visual inspection of the droplets confirms this.

We used both ridged and pillared surfaces in our simulations (see Fig. 3). The ridged surface consisted of straight, raised ridges with period L arranged perpendicular to the surface normal and the direction of the body force. The pillared surface consisted of raised posts, arranged in a square lattice with period L . The atoms comprising the posts themselves were arranged in four layers of two particles, with the atoms occupying opposing corners of a cube with side length $\frac{1}{\sqrt{2}}$ in a tetrahedral fashion. The exact dimensions are detailed in Table I and shown in panels (a) and (b) of Fig. 3.

The temperature was controlled by a Langevin thermostat [31] applied to all fluid particles in the direction perpendicular to the surface normal and the direction of the body force with a set temperature of $0.63 \epsilon k_B^{-1}$. This temperature was chosen to ensure that the droplet was liquid for the range of droplet sizes

TABLE I. The dimensions of the ridged and pillared surfaces used (see Fig. 3), approximating the effective surface particle diameter as 1σ . The period L of the pattern was 3σ for the ridged surface and 4σ for the pillars.

	Height, h	Width, w	Period, L	Area fraction, ϕ
Ridges	2σ	1σ	3σ	0.33
Pillars	3.328σ	1.707σ	4σ	0.18

investigated, which was checked by reference to the radial distribution functions for particles in the droplet. Vapor was present in equilibrium with the rolling droplets.

The surface tension was estimated as $\sim 0.34 \epsilon \sigma^{-2}$ by examining the relationship between drop size to its internal energy [32] at a temperature of $T = 0.63 \epsilon k_B^{-1}$. Again, our estimates are of the same order as those reported elsewhere [33]. The particle density ρ within the droplet was found to be around $1.1\sigma^{-3}$ for the droplet sizes examined here.

There are several ways one can calculate the shear viscosity in bulk fluids using molecular dynamics [34]. However, the droplets in our simulations are undercooled relative to the bulk freezing temperature. This made it difficult to calculate the viscosity in a comparable bulk liquid using a Green-Kubo approach [35,36], as even with a rapid quench, freezing would occur before the calculation converged. Indeed, this temperature and pressure fall outside of the range where viscosities have previously been calculated for the bulk Lennard-Jones liquid [37]. However, by observing the exponential decay of the Green-Kubo time correlation function in a quenched bulk liquid (at $T = 0.63 \epsilon k_B^{-1}$ and particle density $\rho \approx 1.09 \sigma^{-3}$) prior to freezing, we estimate a viscosity of $15 \pm 8 \epsilon \sigma^{-3} \tau$. One could measure self-diffusion within the droplets themselves and then estimate the viscosity using the Stokes-Einstein relation [38], but particles in the droplet are exchanged with the vapor sufficiently rapidly to bias the corresponding mean-square displacements (particles that move further are more likely to be ejected), resulting in estimates of the viscosity that are too large. Nonetheless, the atomic mean-square displacement within the bulk liquid prior to freezing gave an estimate of the viscosity of $8 \pm 4 \epsilon \sigma^{-3} \tau$.

Droplets were equilibrated by monitoring temperature and mass prior to the application of the body force. For production runs, with the body force on, we monitored the center-of-mass velocities and droplet masses to ensure the flow reached steady state. Position and velocity data for particles were collected over 10^6 time steps once droplets reached steady-state motion. Steady-state motion was generally reached between 10^4 and 10^6 time steps for the smallest and largest droplets, respectively, for the range of body forces g used in this work. The droplets were determined to be in the Cassie-Baxter state by computing the vapor density in regions between the pattern features below the droplet. The particles in the droplet (as opposed to those in the vapor, as illustrated in Fig. 3) were identified in postprocessing using a distance-threshold approach, with all droplet mass, density, radius, and motion statistics being calculated from the distribution of positions and velocities belonging to the associated particles.

Velocity profiles describing the average velocity of the droplet as a function of height were constructed by time-averaging the velocity in the x direction $u_x(z)$ within horizontal x - y sections, sliced at 1σ intervals along the z axis, for each droplet. As discussed in the previous section, the model assumes that the internal motion of the droplet resembles a pure rotation plus some shear near the contact zone. Indeed, as shown in Fig. 4, apart from the presence of slip, this model seems to provide a very good description of the motion: relative to the center-of-mass velocity, the residual velocity profile varies linearly with height indicating a rolling motion, with a deviation from this near the substrate where shear is

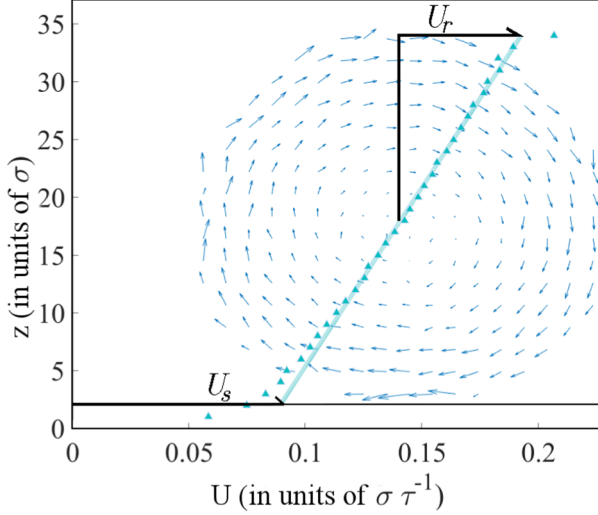


FIG. 4. The time-averaged velocity field (relative to the center-of-mass velocity) and average velocity profile for a droplet ($R = 16\sigma$) in steady-state motion on a ridged surface with $g = 5.7 \times 10^{-4} \sigma \tau^{-2}$ and $\epsilon_{\text{SL}} = 0.07\epsilon$. A straight line has been fitted to the top half of the profile to calculate the rolling velocity U_r (projected toward the surface for reference). A nonzero slip velocity U_s is evident at the pattern surface (indicated by the solid line at $z = 2\sigma$).

evident. As such, a linear fit was made to the top half of each velocity profile (computed from the average velocity of atoms within a 1σ -thick slice as a function of height z above the base of a ridged substrate) to calculate the rolling velocity U_r . The slip velocity was then calculated as $U_s = U - U_r$, where U is the center-of-mass velocity of the droplet.

In the graphs that follow, standard errors are calculated for the droplet velocity data. While the time-averaged droplet velocity remains relatively consistent between simulation runs, within a simulation distinct periods of rolling-dominated and slip-dominated motion can be observed, as is evident in Fig. 5.

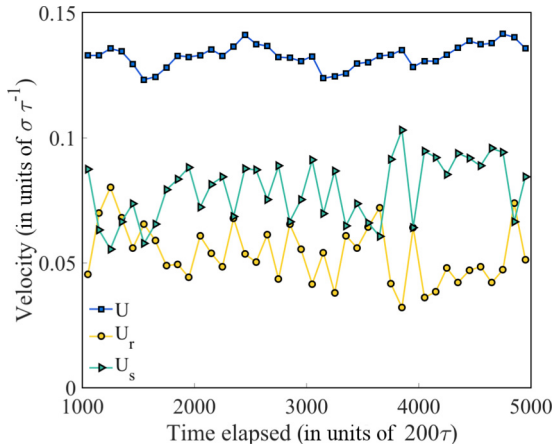


FIG. 5. The evolution of U , U_r , and U_s over the course of a single simulation run for a 16σ droplet on a ridged surface is shown. Each point was calculated using averages of 100 consecutive frames of data, with frames generated every 200 time steps. While U remains reasonably consistent, varying by up to 5% relative to the mean, U_r (and by extension U_s) varies by as much as 30%.

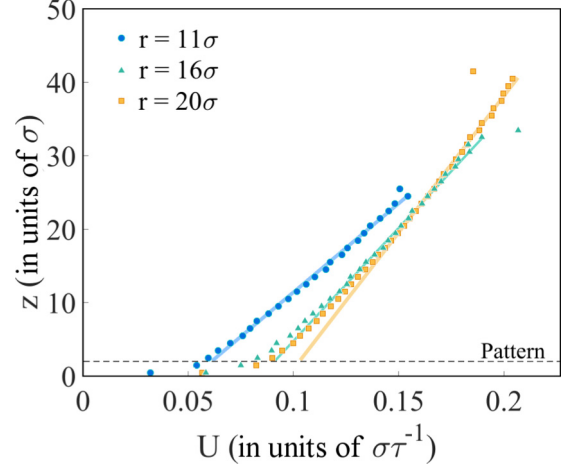


FIG. 6. The velocity profiles of droplets with initial radii of 11σ (blue circles), 16σ (green triangles), and 20σ (orange squares) in steady-state motion on a ridged surface with $g = 5.7 \times 10^{-4} \sigma \tau^{-2}$ and $\epsilon_{\text{SL}} = 0.07\epsilon$. Straight lines have been fitted to the velocities as in Fig. 4, illustrating deviations from a purely rolling motion. The resulting shear becomes more apparent as the droplet size increases.

As such, there is an additional source of temporal variability in U_r and U_s that has not been captured in the errors presented here.

III. RESULTS

The steady-state velocity profiles for three drops with differing radii ($R = 11\sigma$, 16σ , and 20σ) simulated with $\epsilon_{\text{SL}} = 0.07\epsilon$ (unless otherwise stated, this value of ϵ_{SL} is used throughout) on a ridged substrate tilted at an angle $\alpha = 10^\circ$ with $g = 5.7 \times 10^{-4} \sigma \tau^{-2}$ are shown in Fig. 6. The larger drops have a higher steady-state velocity than the smaller drops, with U_s (the velocity at the top of the patterned surface) increasing as the droplet size increases, while U_r (which is proportional to the slope of the linear profile) remains relatively constant with size. Similar results are obtained on surfaces with pillars.

Figure 7 shows steady-state center-of-mass velocities U , now decomposed into U_s and U_r , for a wider size range of droplets on ridged surfaces ($R = 9\sigma - 31\sigma$) with the same g . We note a steady increase in U with droplet size up to about $R \sim 20\sigma$. Above this radius, the velocity plateaus as the droplet radius approaches the capillary length. At this point, the droplet starts to deviate from its spherical shape (here both Re and We approach unity). Up to this point, the increase in velocity with droplet size is very different from the behavior predicted by Eq. (3). We also note that it is largely the slip velocity U_s that increases with droplet size.

Switching to a pillared surface, Fig. 8 shows U for a 16σ radius droplet as the magnitude of body force g is changed. For small g ($\leq 1.14 \times 10^{-3} \sigma \tau^{-2}$) we find that the simulated velocity scales close to \sqrt{g} (fitting with a power-law fit yields an exponent 0.59). Above this threshold, the dependence on g is much weaker. We note that the magnitude of g affects the capillary length, and given the droplet radius of $R = 16\sigma$, we expect the droplet to lose its spherical shape for values

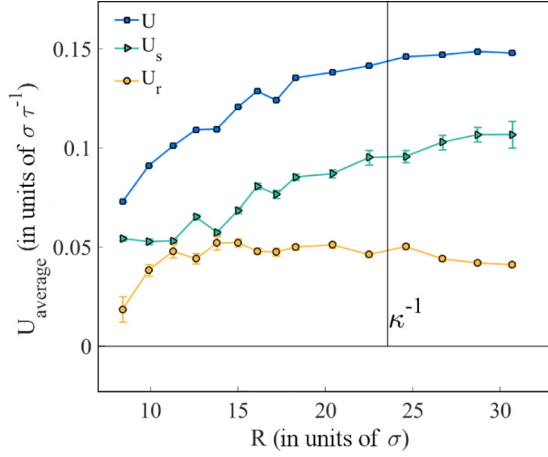


FIG. 7. Plot of time-averaged droplet center-of-mass velocities U vs the various droplet radii on a ridged surface with $g = 5.7 \times 10^{-4} \sigma \tau^{-2}$ and $\epsilon_{\text{SL}} = 0.07\epsilon$. Droplets larger than the radius indicated by the right-hand vertical line are larger than the capillary length κ^{-1} and so they can be expected to deform and depart from spherical shape assumed by the model. Error bars are determined by the standard error associated with the U values taken from 4000 simulation frames, and U_s and U_r as constructed from 40 100-frame bins.

of g exceeding $\frac{\gamma}{\rho R^2} = 1.14 \times 10^{-3} \sigma \tau^{-2}$. This transition is reflected in the loss of linearity for the two highest values of g that were simulated: 2.3 and $4.6 \times 10^{-3} \sigma \tau^{-2}$.

Figure 9 illustrates similar scaling behavior for droplets on the ridged surface for a range of droplet sizes. In this figure, we have plotted U/R versus g on log-log axes to demonstrate that the $U \sim R/\kappa^{-1}$ scaling holds for droplets with radius $R = 10 - 18\sigma$ (albeit noting the one outlier for the $R = 10\sigma$ droplet under very weak body force, where we observed that the droplet has a tendency to bounce). We note that this scaling is the inverse of the scaling behavior predicted by Eq. (3).

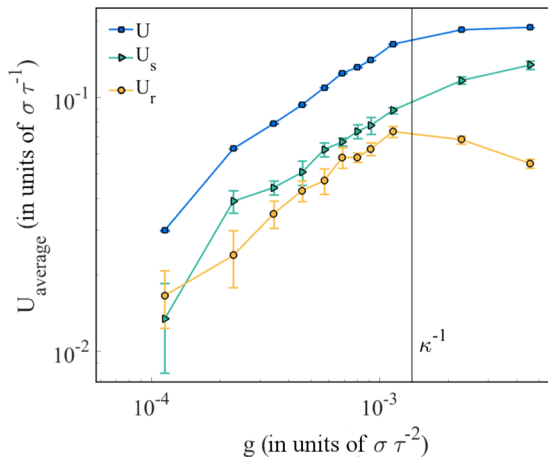


FIG. 8. A log-log plot of the steady-state center-of-mass velocities for droplets with radii fixed at 16σ and $\epsilon_{\text{SL}} = 0.07\epsilon$, as g is increased from 5.7×10^{-5} to $5.7 \times 10^{-3} \sigma \tau^{-2}$. The simulations were performed on the pillared surface. The apparent linear region between $\sim 2.3 \times 10^{-4} \sigma \tau^{-2}$ and $1.14 \times 10^{-3} \sigma \tau^{-2}$ corresponds to a power law $U \propto g^\beta$ with an exponent $\beta \approx 0.59$. Error bars are calculated as in Fig. 7.

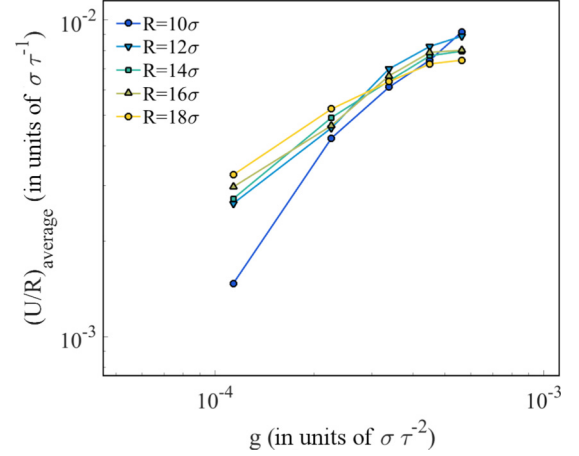


FIG. 9. The steady-state center-of-mass droplet velocities scaled by radius for radii between 10σ and 18σ on a ridged surface with $\epsilon_{\text{SL}} = 0.07\epsilon$, as g is increased from 1.14×10^{-4} to $5.7 \times 10^{-4} \sigma \tau^{-2}$. The log-log plot confirms the R/κ^{-1} scaling of the center-of-mass velocity for droplets smaller than the capillary length. The standard errors, calculated as in Fig. 7, are too small to be visible.

For the majority of results presented above, we used a value of $\epsilon_{\text{SL}} = 0.07\epsilon$, but Fig. 10 shows how U varies as ϵ_{SL} is varied between 0.05ϵ and 0.14ϵ for the ridged surface. We also note a steady decrease in U and U_s , while U_r remains approximately constant. Simulations on the equivalent pillared surfaces show similar behavior. Equation (3) does not make predictions about how U should change with solid-liquid interaction strength, but as ϵ_{SL} increases, some of the approximations that lead to this equation and to aspects of the theory developed below (such as the spherical cap approximation) would be expected to lose validity.

Simulations performed on the ridged and pillared surfaces exhibit similar linear scaling with R , although the center-of-mass velocities for droplets on pillared surfaces are larger, all else being equal. This is expected, given that our pillared

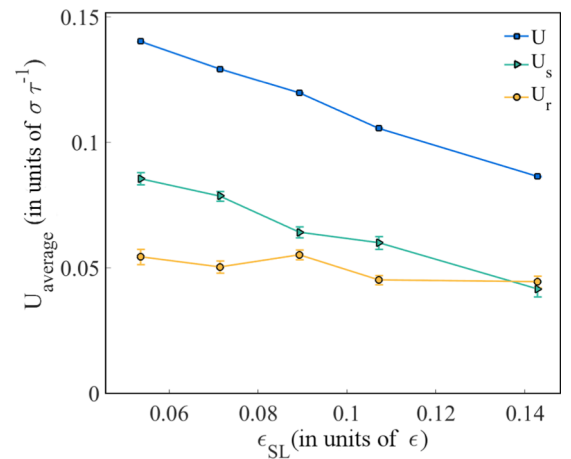


FIG. 10. U and U_s are found to decrease as the strength of the liquid interaction with the ridged surface, characterized by ϵ_{SL} , grows larger. Here, g is $5.7 \times 10^{-4} \sigma \tau^{-2}$ and R is 16σ . Error bars are calculated as in Fig. 7.

surfaces have a lower area fraction ϕ relative to the ridged surfaces, as shown in Table I. Droplets on the pillared and ridged surfaces exhibited similar behavior with respect to the body force until the capillary length approaches the radius of the droplet. This limit is outside the scope of the models developed here, but it may be due to the anisotropy of the ridged surface becoming more important as the droplet begins to puddle.

IV. EXTENDED MODELS

The molecular-dynamics simulations in the previous section show that the droplet is slipping in the contact region, something that is not taken into account in Eq. (3). To incorporate slip into our theoretical treatment, we return to the model of Mahadevan and Pomeau [13], and we introduce an effective Navier slip boundary condition. This condition relates the slip velocity U_s at the surface to the velocity gradient near the contact zone: $U_s = b|\nabla u|_s$, so that $U_s = U_r b/R$ and $U \sim U_r(1 + b/R)$. The condition is assumed to hold over the surface of the contact region. If $R \gg b$, then $U_s/U_r \rightarrow 0$ and we recover the model of Mahadevan and Pomeau.

Here the slip length b should be considered an effective slip length [11,28], i.e., the slip length of some homogeneous surface that would result in the same frictional shear as the inhomogeneous superhydrophobic surface when averaged over a sufficiently large area. For our purposes, the use of an effective slip length is justified provided the size of the contact region, ℓ , is much larger than the structuring of the superhydrophobic surface. For a surface composed of arrays of posts, with post spacing L , the effective slip length b is expected to scale as $L/\phi^{1/2}$, where ϕ is the area fraction of the surface covered by the pillars [11]. In this case, we are justified in using an effective slip length provided $\ell \gg L \sim \phi^{1/2}b$.

We begin by writing the center-of-mass velocity U as the sum of the rolling velocity and the slip velocity: $U = U_r + U_s$. As with Eq. (1), the viscous dissipation is given by

$$P_v = \int_V \mu (\nabla u)^2 dV \sim \ell^3 \mu \left(\frac{U_r}{R} \right)^2, \quad (5)$$

which is balanced by the rate of loss of gravitational potential energy in the steady state:

$$\rho g \sin(\alpha) U R^3 \sim \frac{\ell^3 \mu}{R^2} U^2 \left(1 + \frac{b}{R} \right)^{-2}. \quad (6)$$

This leads to the following expression for the steady-state velocity U :

$$U \sim \frac{\gamma}{\mu} \frac{\kappa^{-1}}{R} (1 + b/R)^2 \sin(\alpha). \quad (7)$$

Note that the droplet velocity is inversely proportional to the droplet radius R [as in Eq. (3)], with a correction due to slip that scales as b/R to leading order. In the limit of small slip, $b \ll R$, the expression for the velocity U reduces to that of Mahadevan and Pomeau [13] plus corrections of order b/R :

$$U \sim \frac{\gamma}{\mu} \frac{\kappa^{-1}}{R} \sin(\alpha) + O(b/R). \quad (8)$$

In the large slip limit, $b \gg R$, the expression suggests that $U \sim \frac{\gamma}{\mu} \frac{\kappa^{-1} b^2}{R^3} \sin(\alpha)$. It will be shown later that in the large slip limit, viscous dissipation will not be the dominant mechanism. Regardless, neither of these expressions describes the increase in steady-state velocity with R and g that was seen in the simulations from the previous section (Fig. 9). We now consider two other potential sources of dissipation: interfacial friction, associated with fluid sliding over the surface, and contact-line friction, due to contact-line pinning-depinning at surface features. The rate of dissipation due to interfacial friction over the contact zone surface can be expressed as

$$P_f = \int_A \sigma_s U_s dA, \quad (9)$$

where σ_s is the shear stress at the contact zone surface, and the integral is taken over this surface. The shear stress at the contact surface is given by the Navier slip-boundary condition: $\sigma_s = \mu |\nabla u| = (\mu/b) U_s$. Thus we estimate

$$P_f = \frac{\mu}{b} \int_A U_s^2 dA \sim \ell^2 \frac{\mu}{b} U_s^2. \quad (10)$$

Along the contact line, the dissipation can be written as [39]

$$P_c = \int_c \zeta U_s^2 dl \sim \ell \zeta U_s^2, \quad (11)$$

where ζ is an effective contact-line friction coefficient, and the integral is taken over the contact line perimeter.

It is worth emphasizing that each of these dissipative mechanisms scales differently with the size of the contact zone ℓ . The rate of energy dissipation associated with the contact line is proportional to ℓ , while dissipation due to interfacial friction is proportional to ℓ^2 and viscous dissipation is proportional to ℓ^3 . As ℓ is related to the size of the droplet ($\ell \sim R^2/\kappa^{-1}$), we might expect different mechanisms to dominate at different droplet sizes. For example, the ratio of the rate of interfacial frictional dissipation to the rate of viscous dissipation is given by

$$\frac{P_f}{P_v} \sim \frac{b}{\ell} \sim \frac{b \kappa^{-1}}{R^2}, \quad (12)$$

so when $\ell \gg b$, the frictional term will become unimportant. Thus viscous dissipation will dominate only when $b \ll \ell$ or $b \ll \ell \sim R^2/\kappa^{-1} \ll R$.

Similarly, the ratio of the rate of contact line dissipation to that due to interfacial friction is given by

$$\frac{P_c}{P_f} \sim \frac{\zeta b}{\mu \ell} \sim \frac{\zeta}{\mu} \frac{b \kappa^{-1}}{R^2}. \quad (13)$$

Thus, the importance of contact line dissipation depends on the ratio of ζ/μ , in addition to the droplet size R and slip length b . We would expect contact line dissipation to dominate when both $b \gg \ell$ and $\zeta/\mu \gtrsim 1$.

We now examine two limiting cases for steady-state droplet motion, where either interfacial friction or contact-line dissipation dominates the balance with gravitational potential energy loss. In the first case, which would require $\mu/\zeta \gg b/\ell \gg 1$, dissipation due to interfacial friction will dominate,

leading to the following balance:

$$\rho g \sin(\alpha) U R^3 \sim \ell^2 \frac{\mu}{b} U^2 \left(1 + \frac{R}{b}\right)^{-2}. \quad (14)$$

This gives

$$U \sim \frac{\gamma}{\mu} \frac{R}{b} (1 + b/R)^2 \sin(\alpha). \quad (15)$$

Here we see that the velocity is proportional to the droplet radius for small slip $b \ll R$ but inversely proportional to the radius for large slip $b \gg R$. (We note that use of an effective slip length in this large slip limit is justified for a surface with posts provided $b \sim L/\phi^{1/2} \gg \ell \gg L$.) Interestingly, the steady-state velocity is independent of the capillary length, so it does not scale with g . This independence is somewhat counterintuitive (and it is not consistent with what is observed in the simulations, as is evident from Fig. 9), but it arises because the frictional losses scale with g in the same way as the loss of gravitational potential energy.

The remaining limit is one in which contact-line dissipation dominates the balance (e.g., when $b \gg \ell$ and $\zeta \gtrsim \mu$):

$$\rho g \sin(\alpha) U R^3 \sim \ell \zeta U^2 \left(1 + \frac{R}{b}\right)^{-2} \quad (16)$$

resulting in

$$U \sim \frac{\gamma}{\zeta} \frac{R^3}{b^2 \kappa^{-1}} (1 + b/R)^2 \sin(\alpha). \quad (17)$$

In this case, the steady-state velocity is inversely proportional to the capillary length, so it scales as $U \sim \sqrt{g}$, which is consistent with the behavior observed in Fig. 8. In the low slip limit ($b \ll R$) the velocity is proportional to the droplet volume, while in the high slip limit ($b \gg R$) it is proportional to the droplet radius (as seen in Fig. 7 for droplets with radii below the capillary length).

Ideally, one would compute the viscosity and slip length b in independent simulations to determine the appropriate flow regime and check consistency with the scaling arguments. However, as discussed above, the small size of the droplets makes it difficult to compute the viscosity directly. More importantly, the undercooling of the droplets relative to the bulk means we are not able to independently calculate slip lengths in a Couette or Poiseuille-type flow. Instead, our strongest test for the theory is the observation of how the simulated center-of-mass velocities scale with the droplet size and gravitational force.

Indeed, it is evident that the scaling of the simulated U is best explained by contact-line dissipation in the high slip limit. In this limit, we expect $U \sim \frac{\gamma}{\zeta} \frac{R}{\kappa^{-1}} \sin(\alpha) + O(R/b)$. Of the dissipation mechanisms explored above, only this expression is consistent with both an increase in droplet speed with radius and an increase in speed with the strength of the gravitational body force that was observed in the simulations. This is also consistent with the decrease in U observed as ϵ_{SL} increases (Fig. 10), as increasing the strength of the solid-liquid interaction will also cause ζ to increase.

We can also check post hoc that the observed scaling of U is consistent with estimates of the magnitude of the slip length from the simulations themselves. Calculating the slip length

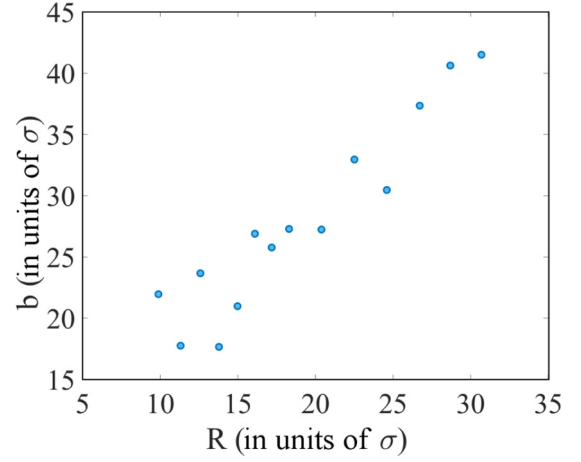


FIG. 11. The estimated effective slip length $b \sim \frac{RU_s}{U_r}$ increasing with increasing droplet radius calculated for the U_s and U_r data shown in Fig. 7 (on a ridged surface, with $g = 5.7 \times 10^{-4} \sigma \tau^{-2}$ and $\epsilon_{SL} = 0.07\epsilon$). We interpret the increase in effective slip length with ϵ as a decreasing contribution of the contact-line friction as the droplet size increases.

here is not straightforward (while U_s is accessible, reliably estimating the shear at the surface is difficult), but we note that we can estimate b from the approximation $U_s = b|\nabla u| \sim b(U_r/R)$, i.e., $b \sim RU_s/U_r$. This suggests that $b \sim 20 - 40\sigma \gtrsim R$, as shown in Fig. 11, indicating that the droplets are experiencing high slip. These effective slip lengths are consistent with the range of values reported by Cottin-Bizonne *et al.* [40]. A striking feature of Fig. 11 is the increase in effective slip length b with droplet size. We attribute this increase to the increasing importance of contact-line friction as droplets get smaller, which is not explicitly captured in the Navier slip boundary condition but will likely enter as an effective contribution to the interfacial friction that scales as the ratio of contact zone perimeter to contact zone area. Using these estimates of the slip length, and the computed velocities, we can use Eq. (17) to estimate a lower bound for $\zeta \sim O(1)\epsilon\sigma^{-3}$.

V. DISCUSSION

It is interesting to consider the experimental application of the models developed in the previous section. Using molecular kinetic theory to describe the contact-line dynamics [17,19], an indicative value of the contact-line friction parameter ζ for water on polyethylene terephthalate (contact angle 82°) is 0.01 Pa s [19], giving $\zeta/\mu \sim O(10)$. However, in molecular kinetic theory, ζ depends strongly on the contact angle θ_c [18]:

$$\zeta = \zeta_0 \exp\left(\frac{\gamma \lambda^2 \cos(\theta_c)}{k_B T}\right), \quad (18)$$

where ζ_0 is the value of the friction coefficient at 90° , and λ is a molecular “hopping” distance. Taking $\zeta_0 = 0.01 \text{ Pa s}$ and $\lambda = 0.3 \text{ nm}$, we estimate $\zeta/\mu \sim O(1)$ for water with a contact angle of 180° at room temperature.

Furthermore, ζ has generally been found to scale proportionally with μ for different fluids [18], so a situation in which $\zeta \ll \mu$ seems unlikely. Thus we conclude that droplet motion

is unlikely to be dominated by interfacial friction even in the limit of large slip (as noted earlier, effective slip lengths on highly engineered superhydrophobic surfaces have been measured to be as large as $200\ \mu\text{m}$ [12]). For water on a superhydrophobic surface, the steady-state motion will either be dominated by viscous shear (when $b \ll \ell$) or by contact line dissipation (when $b \gg \ell$), or all three forms of dissipation will be important (when $b \sim \ell$). It is possible that on close to ideal superhydrophobic surfaces, such as SLIPS surfaces [41], interfacial friction may become more important than contact-line dissipation.

VI. CONCLUSION

In conclusion, we have extended a prior theoretical treatment of steady-state droplet motion on tilted superhydrophobic surfaces [13] to account for interfacial and contact-line friction. We have investigated limiting cases in which droplet motion is dominated by viscous dissipation, interfacial friction, or contact-line dissipation in turn. In contrast to the predictions of prior models that neglect slip, molecular-dynamics simulations of droplets on tilted superhydrophobic surfaces

reveal a mixture of slipping and rolling motion. The scaling behavior of the simulated droplets with radii less than the capillary length suggests that the steady-state motion is dominated by contact-line dissipation. On leaves, droplet motion is likely to be dominated by viscous dissipation, and slip can likely be neglected. Contact-line dissipation, however, is likely to be important for highly engineered surfaces with high slip lengths, while interfacial friction may be important on close to ideal surfaces that lack features for contact-line pinning to occur.

ACKNOWLEDGMENTS

The authors thank the MacDiarmid Institute for Advanced Materials and Nanotechnology for funding. The authors also wish to acknowledge the contribution of NeSI high-performance computing facilities to the results of this research. New Zealand's national facilities are provided by the New Zealand eScience Infrastructure and funded jointly by NeSI's collaborator institutions and through the Ministry of Business, Innovation & Employment's Research Infrastructure programme (<https://www.nesi.org.nz>).

-
- [1] W. Barthlott and C. Neinhuis, *Planta* **202**, 1 (1997).
 - [2] C. Neinhuis and W. Barthlott, *Ann. Bot.* **79**, 667 (1997).
 - [3] A. Lafuma and D. Quere, *Nat. Mater.* **2**, 457 (2003).
 - [4] A. Fritsch, G. Willmott, and M. Taylor, *J. R. Soc. N. Z.* **43**, 198 (2013).
 - [5] D. Quere, *Rep. Prog. Phys.* **68**, 2495 (2005).
 - [6] D. Richard and D. Quere, *Europhys. Lett.* **48**, 286 (1999).
 - [7] C. Cottin-Bizonne, J.-L. Barrat, L. Bocquet, and E. Charlaix, *Nat. Mater.* **2**, 237 (2003).
 - [8] J. P. Rothstein, *Annu. Rev. Fluid Mech.* **42**, 89 (2010).
 - [9] C. H. Choi and C. J. Kim, *Phys. Rev. Lett.* **96**, 066001 (2006).
 - [10] P. Joseph, C. Cottin-Bizonne, J. M. Benoît, C. Ybert, C. Journet, P. Tabeling, and L. Bocquet, *Phys. Rev. Lett.* **97**, 156104 (2006).
 - [11] C. Ybert, C. Baretin, C. C. Bizonne, P. Joseph, and L. Bocquet, *Phys. Fluids* **19**, 123601 (2007).
 - [12] C. Lee, C. H. Choi, and C. J. C. Kim, *Phys. Rev. Lett.* **101**, 064501 (2008).
 - [13] L. Mahadevan and Y. Pomeau, *Phys. Fluids* **11**, 2449 (1999).
 - [14] N. Moradi, F. Varnik, and I. Steinbach, *Europhys. Lett.* **95**, 44003 (2011).
 - [15] M. Sakai, J.-H. Song, N. Yoshida, S. Suzuki, Y. Kameshima, and A. Nakajima, *Langmuir* **22**, 4906 (2006).
 - [16] M. Sakai, H. Kono, A. Nakajima, X. Zhang, H. Sakai, M. Abe, and A. Fujishima, *Langmuir* **25**, 14182 (2009).
 - [17] T. D. Blake and J. M. Haynes, *J. Colloid Interface Sci.* **30**, 421 (1969).
 - [18] T. D. Blake and J. D. Coninck, *Adv. Colloid Interface Sci.* **96**, 21 (2002).
 - [19] T. D. Blake, *J. Colloid Interface Sci.* **299**, 1 (2006).
 - [20] P. Olin, S. B. Lindström, T. Pettersson, and L. Wågberg, *Langmuir* **29**, 9079 (2013).
 - [21] H.-J. Butt, N. Gao, P. Papadopoulos, W. Steffen, M. Kappl, and R. Berger, *Langmuir* **33**, 107 (2017).
 - [22] J. Servantie and M. Moller, *J. Chem. Phys.* **128**, 014709 (2008).
 - [23] S. R. Annapragada, J. Y. Murthy, and S. V. Garimella, *Int. J. Heat Mass Transf.* **55**, 1457 (2012).
 - [24] B. M. Mognetti, H. Kusumaatmaja, and J. M. Yeomans, *Faraday Discuss.* **146**, 153 (2010).
 - [25] Z. Li, G. H. Hu, Z. L. Wang, Y. B. Ma, and Z. W. Zhou, *Phys. Fluids* **25**, 072103 (2013).
 - [26] Ø. Wind-Willassen and M. P. Sørensen, *Eur. Phys. J. E* **37**, 65 (2014).
 - [27] G. Karapetsas, N. T. Chamakos, and A. G. Papathanasiou, *J. Phys. Condens. Matter* **28**, 085101 (2016).
 - [28] S. C. Hendy and N. J. Lund, *Phys. Rev. E* **76**, 066313 (2007).
 - [29] S. J. Plimpton, *J. Comput. Phys.* **117**, 1 (1995).
 - [30] X. Yong and L. T. Zhang, *Langmuir* **25**, 5045 (2009).
 - [31] T. Schneider and E. Stoll, *Phys. Rev. B* **17**, 1302 (1978).
 - [32] J. W. Lee and G. D. Stein, *J. Phys. Chem.* **91**, 2450 (1987).
 - [33] J. J. Potoff and A. Z. Panagiotopoulos, *J. Chem. Phys.* **112**, 6411 (2000).
 - [34] B. Hess, *J. Chem. Phys.* **116**, 209 (2002).
 - [35] R. Rowley and M. Painter, *Int. J. Thermophys.* **18**, 1109 (1997).
 - [36] K. Tankeshwar, K. Pathak, and S. Ranganathan, *J. Phys. C* **21**, 3607 (1988).
 - [37] V. G. Baidakov, S. P. Protsenko, and Z. R. Kozlova, *Chem. Phys. Lett.* **517**, 166 (2011).
 - [38] F. Varnik and K. Binder, *J. Chem. Phys.* **117**, 6336 (2002).
 - [39] F. Brochard-Wyart and P. de Gennes, *Adv. Colloid Interface Sci.* **39**, 1 (1992).
 - [40] C. Cottin-Bizonne, C. Barentin, É. Charlaix, L. Bocquet, and J.-L. Barrat, *Eur. Phys. J. E* **15**, 427 (2004).
 - [41] T.-S. Wong, S. H. Kang, S. K. Tang, E. J. Smythe, B. D. Hatton, A. Grinthal, and J. Aizenberg, *Nature (London)* **477**, 443 (2011).